ACS APPLIED NANO MATERIALS
Cite This: ACS Appl. Nano Mater. 2019, 2, 4547−4555
Article
www.acsanm.org

Thick Transparent Nanoparticle-Based Mesoporous Silica Monolithic Slabs for Thermally Insulating Window Materials

Michal Marszewski,[†] Sophia C. King,[‡] Yan Yan,[‡] Tiphaine Galy,[†] Man Li,[†] Ali Dashti,[†] Danielle M. Butts,[§] Joon Sang Kang,[†] Patricia E. McNeil,[§] Esther Lan,[§] Bruce Dunn,[§,∥] Yongjie Hu,[†] Sarah H. Tolbert,[‡,§,∥] and Laurent Pilon*[,†,∥,⊥]

[†]Mechanical and Aerospace Engineering Department, [‡]Department of Chemistry and Biochemistry, [§]Department of Materials Science and Engineering, [∥]California NanoSystems Institute, and [⊥]Institute of the Environment and Sustainability, University of California, Los Angeles, Los Angeles, California 90095, United States

Supporting Information

ABSTRACT: This paper presents a novel template-free water-based sol−gel method to synthesize thick transparent and thermally insulating mesoporous silica monolithic slabs by gelation and drying of a colloidal suspension of silica nanoparticles under ambient conditions. For the first time, mesoporous silica slabs were synthesized on perfluorocarbon liquid substrates to reduce adhesion and enable the gels to shrink freely during aging and drying without incurring significant stress that could cause fracture. The free-standing nanoparticle-based mesoporous silica slabs were disks or squares, with thickness between 1 and 6 mm and porosity around 50%. The slabs had high transmittance and low haze in the visible spectrum due to small nanoparticles (6−12 nm) and pore size (<10 nm), narrow pore size distribution, and optically smooth surfaces (roughness <15 nm). The slabs' effective thermal conductivity of 104−160 mW m^{-1} K^{-1} at room temperature was smaller than that of other mesoporous silicas with similar or even larger porosity reported in the literature. This was attributed to the slabs fractal structure and high mass fractal dimension. The mechanical properties were similar to those of common polymers. The simple synthesis is readily scalable and offers promising materials for window solutions and solar−thermal energy conversion, for example.

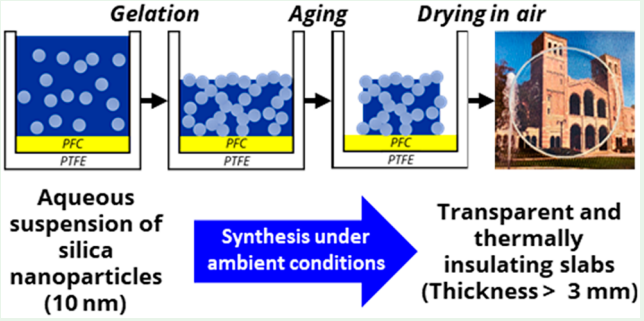

KEYWORDS: *mesoporous silica, silica nanoparticles, optically transparent thermal insulators, transparent slabs, liquid substrates*

1. INTRODUCTION

Mesoporous silica monoliths can take various shapes (e.g., slabs, discs, and rods)[1] and feature large specific surface area and porosity, small pore size (2−50 nm), low effective thermal conductivity, and low dielectric constant.[2] They have been commonly used in adsorption,[3−6] catalysis,[6−8] and chromatography[9−13] for their large surface area and porosity. Recently, transparent mesoporous silica monoliths have found applications as optically transparent supports in photocatalysis,[14] optics,[15] and laser amplification.[16] They have also been used as ultralow refractive index substrates for waveguides[17] and as optically transparent thermal insulation in window solutions[18,19] and in solar−thermal energy conversion.[20−24]

Mesoporous silica films or powders are often prepared by using sol−gel methods.[25] The synthesis typically uses organic templates (e.g., surfactants or block copolymers) that form mesopores with controlled shape and diameter between 1.5 and 30 nm[26,27] and porosity up to 80%.[27] However, mesoporous silica monoliths are much more difficult to synthesize by a sol−gel method because the silica network is subjected to significant capillary forces during evaporation of the solvent present in the mesopores. These forces impose enormous stress on the silica network, causing it to shrink during aging and drying.[25] If the stress exceeds the compressive strength of the gel, the monolith cracks and may crumble into powder.

Synthesis of thick mesoporous silica monolithic slabs that are both transparent and thermally insulating is even more challenging.[28] First, achieving low thermal conductivity requires large porosity.[29] Second, transparency requires that the slab's pores and surface roughness be much smaller than the wavelength of the incident visible light (400−700 nm) so as to minimize volumetric and surface scattering responsible for haze. However, mesoporous silica slabs with large porosity also tend to have larger pores that scatter light.[30] For example, aerogels with porosity exceeding 80% have low thermal conductivity but are typically hazy because of their wide pore size distribution with some pores exceeding 40 nm in

Received: May 13, 2019
Accepted: July 1, 2019
Published: July 15, 2019

DOI: 10.1021/acsanm.9b00903
ACS Appl. Nano Mater. 2019, 2, 4547−4555

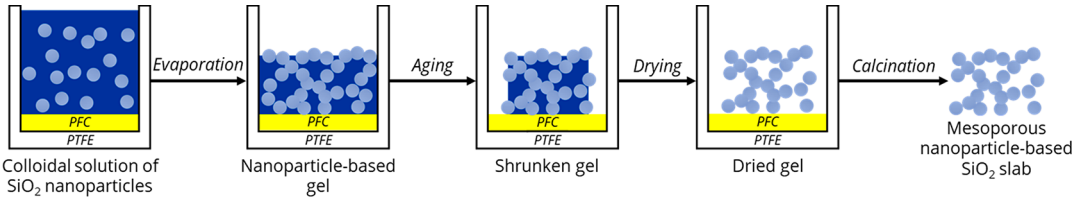

Figure 1. Scheme of the sol–gel synthesis of thick transparent nanoparticle-based mesoporous silica monolithic slabs on a PFC liquid substrate.

diameter.[31] Third, in addition to capillary forces and stress caused by evaporation, mesoporous silica slabs synthesized by using sol–gel method may crack due to adhesion forces pinning the gel to the substrate.[25] All mesoporous silica gels undergo significant shrinkage during aging and drying.[25] Because gels are soft and fragile, opposing adhesion and compressive forces due to shrinkage almost inevitably result in cracking.[25] In fact, adhesion forces are proportional to the footprint surface area of the gel, making it especially challenging to synthesize large slabs.

Several solutions to the cracking of mesoporous silica monoliths have been proposed. The two most common strategies include (i) supercritical drying[25] and (ii) ambient drying by solvent exchange[32−35] of aged gels. Both strategies consist of exchanging water contained in the pores for a liquid with lower surface tension to minimize capillary forces. Both processes lead to mesoporous silica monoliths, but their scale-up is rendered difficult by the facts that (i) supercritical drying requires expensive high-pressure equipment and (ii) ambient drying may be time-consuming and requires large volumes of organic solvents used in solvent exchange.

Synthesis of mesoporous silica monoliths can also be achieved by (1) scaffolding silica network with a secondary material[36−42] or by (2) inducing flexibility in the silica network.[43−46] In the first method, a composite monolith is prepared that contains silica and a secondary material (e.g., carbon,[36] polymers,[37−40] nanofibril cellulose,[41] or silica nanowires[42]) that serves as a scaffold supporting the silica network and preventing cracking upon drying.[42] In the second method, flexible mesoporous silica monoliths are fabricated by incorporating organic groups[43,44] and carbon nanotubes[45] or by double cross-linking of silica and organic networks.[46] Such flexible monoliths shrink without cracking due to their mechanically compliant network, and once completely dry, they spring back to the original size.[47] Although successful, both strategies are complicated to implement and most monoliths prepared by using these methods are opaque.[36−43,45]

Few studies have reported synthesis of transparent (not translucent) mesoporous silica slabs with high transmittance and low haze. Rozière et al.[48] synthesized transparent mesoporous silica slabs by a soft-templating sol–gel synthesis using tetraethyl orthosilicate (TEOS) as the silica precursor and the nonionic surfactant Brij 30 as the template. The resulting gels were calcined at 560 °C to remove the polymer template. Interestingly, other authors have reported cracking of similar soft-templated monoliths after calcination.[49,50] However, Rozière et al.[48] synthesized monoliths that did not crack and were 15 mm in diameter and 3 mm in thickness with porosity around 50% and average pore width of 2.3 nm. Unfortunately, neither the monoliths' thermal conductivity nor their optical properties were reported, even though they appear optically clear.

This paper aims to develop a novel template-free method to synthesize thick transparent and thermally insulating mesoporous silica monolithic slabs made of silica nanoparticles. The nanoscale architecture of the mesoporous slabs was characterized by transmission electron microscopy (TEM), nitrogen porosimetry, small-angle X-ray scattering (SAXS), and surface profilometry. Their transmittance and haze were measured across the visible part of the spectrum while their effective thermal conductivity and effective Young's modulus and hardness were measured at room temperature.

2. EXPERIMENTAL SECTION

2.1. Material Synthesis. Figure 1 shows the general scheme of the synthesis method for nanoparticle-based mesoporous silica slabs on a PFC liquid substrate. The method consists of (1) pouring the nanoparticle suspension into a mold whose bottom is covered with PFC liquid, (2) partly evaporating the water to drive gelation of the suspension, (3) aging of the gel, accompanied by shrinkage, (4) drying of the aged gel until all the water has evaporated, and (5) calcinating the slabs in oxygen at 400 °C for 2 h using a 5 °C min^{-1} temperature ramp to remove NH_3 from the pores and any potential PFC residues from the bottom surface. Here, a commercially available colloidal solution of silica nanoparticles Nalco 2326 (15 wt % in water, NH_3 stabilized, lot number BP7J1239A1, Nalco Chemical Company, Naperville, IL) was used, but in general, the synthesis can be performed using any colloidal silica solution. The PFC liquids used as the liquid substrates were perfluoropolyether oils Krytox GPL 100, GPL 104, and GPL 106 (Miller-Stephenson Chemical Company Inc., Danbury, CT) with general formula $[CF(CF_3)CF_2O]_n$ where n = 10–60. Although these PFC liquids have slightly different molecular weights, they have the same chemical properties and thus were used interchangeably in the experiments. Changing the PFC liquids had no noticeable effect on the synthesized slabs. It is worth mentioning that the PFC liquids were recovered after the synthesis and reused in subsequent experiments since they did not mix with the colloidal solution and could be easily recovered once the solution had gelled. Note that the colloidal solution or gel of silica nanoparticles had an effective density ranging between 1.0 and 1.6 g cm^{-3} and thus floated on the PFC liquid substrate, whose density is 1.9 g cm^{-3}.[51]

For comparison, mesoporous silica slabs were synthesized on a solid PTFE substrate by using the same procedure (Figure 1) except that the colloidal solution of silica nanoparticles was placed in an empty PTFE mold without PFC liquid. The mesoporous slabs prepared on PTFE were analyzed as synthesized, i.e., without calcination.

Nanoparticle-based mesoporous silica slabs synthesized on PFC liquid substrates were labeled as SiO_2-PFC-rt, SiO_2-PFC-40C, and SiO_2-PFC-hc while those synthesized on PTFE substrates were labeled as SiO_2-PTFE-rt, SiO_2-PTFE-40C, and SiO_2-PTFE-hc for slabs dried at room temperature or in an oven at 25 °C, in an oven at 40 °C, and in a humidity chamber at room temperature, respectively. Details of the chemicals, quantities, and synthesis procedure are available in the Supporting Information.

2.2. Characterization Methods. The synthesized nanoparticle-based mesoporous silica slabs were characterized structurally by TEM. Low-temperature nitrogen porosimetry provided specific surface area, total specific pore volume, porosity, micropore volume, pore size distribution, and peak pore width of the mesoporous slabs. Small-

DOI: 10.1021/acsanm.9b00903
ACS Appl. Nano Mater. 2019, 2, 4547–4555

angle X-ray scattering (SAXS) was used to analyze the fractal structure of the materials and to determine the mass fractal dimension. Profilometry gave the average and root-mean-squared surface roughness of the slab surfaces. The spectral normal-hemispherical and diffuse transmittances, haze, and color rendering index of the slabs in the visible spectrum were measured by using a UV−vis spectrometer equipped with an integrating sphere. Time-domain thermoreflectance was used to measure the effective thermal conductivity at room temperature under vacuum or in air. Nanoindentation was performed to retrieve the effective Young's modulus and hardness of the mesoporous slabs. Details of the instrumentation and data analysis are also provided in the Supporting Information.

3. RESULTS AND DISCUSSION

3.1. Synthesis Design. The present synthesis method (Figure 1) resulting in mesoporous silica monolithic slabs that are both transparent and thermally insulating combines several strategies aiming to address challenges in making crack-free highly porous slabs with small pores and optically smooth surfaces. For the first time, synthesis of mesoporous silica monolithic slabs used a PFC liquid substrate to minimize adhesion between the gel and the substrates and to obtain optically smooth surfaces. PFC liquids were selected as substrates because of (i) their omniphobic properties, ensuring immiscibility with the aqueous colloidal solution of silica nanoparticles, (ii) their high density, ensuring that the colloidal solution floated on the liquid substrate, and (iii) large surface tension with water, ensuring flatness of the liquid−liquid interface. The latter enabled the gels to shrink during aging and drying without incurring significant stress that would otherwise lead to fractures. Similar effects were achieved by using the PTFE substrate due to its nonstick properties, but the surface roughness of the PTFE was much greater. Moreover, despite its high chemical inertness, gels still slightly adhered to the PTFE substrate, resulting in lower yield of crack-free slabs. Note that this effect was negligible for slabs with small footprint surface area (<3 cm in diameter). However, larger slabs cracked noticeably more often during aging. By contrast, slabs prepared on PFC liquids did not crack during aging regardless of their size.

In addition, the present synthesis used small silica nanoparticles (6−12 nm in diameter) as the building blocks (i) to avoid large shrinkage during aging and drying and (ii) to ensure that the mesopores created between the nanoparticles were much smaller than the wavelength of visible light so as to minimize light scattering. Nanoparticle-based gels experienced smaller shrinkage than typical gels synthesized from molecular precursors (e.g., TEOS) because (a) virtually all silica is bound in the building blocks rather than dissolved in the solution and (b) there was little room for structural rearrangement and evolution once the network had formed.[25] Most importantly, reactions of residual precursor and unreacted groups that drive shrinkage of typical gels are mostly absent in our nanoparticle-based gels. Conveniently, the reduced shrinkage of nanoparticle-based gels also enabled us to achieve large porosity.

Figure 2 shows optical images of representative thick transparent nanoparticle-based mesoporous silica monolithic slabs: (a) a circular slab with diameter of 3.6 cm and average thickness of 3 mm synthesized on PFC liquid at room temperature (SiO_2-PFC-rt) and (b) a square slab with round corners with size of 2.4 cm and average thickness of 5 mm synthesized on PTFE at room temperature (SiO_2-PTFE-rt). The difference in slabs' size and shape was due to the different molds used in the slab preparation. Here, both cylindrical molds with diameter ranging from 3.8 to 6.2 cm and square molds with a size of 3.4 cm were used (see Figure S1 in the Supporting Information for circular slabs prepared on PTFE). While the final size and shape of the slabs were determined by those of the mold, the average thickness was determined by the initial volume of the colloidal solution of silica nanoparticles. Overall, mesoporous silica monolithic slabs with sizes between 2 and 4.5 cm and thickness between 1 and 6 mm were synthesized. Notably, the SiO_2-PFC-rt slabs had higher transparency than the SiO_2-PTFE-rt slabs. This difference will be discussed in the following sections.

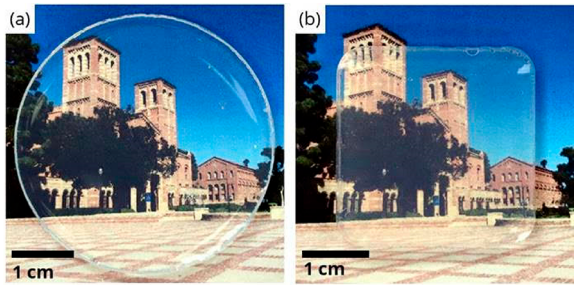

Figure 2. Optical images of representative thick transparent nanoparticle-based mesoporous silica monolithic slabs: (a) a circular slab synthesized on PFC liquid at room temperature and (b) a square slab with round corners synthesized on PTFE at room temperature. The slabs were 3.6 cm in diameter and 2.4 cm in size and had average thickness of 3 and 5 mm, respectively. Note that only the slab in (a) was calcined at 400 °C for 2 h.

3.2. Structural Characterization. Figure 3 shows representative TEM images and particle diameter histograms (insets) of transparent nanoparticle-based mesoporous silica monolithic slabs prepared (a) on PFC liquid and (b) on PTFE. Both types of slabs had similar structures with a network made of aggregated silica nanoparticles. The average diameters of silica nanoparticles were 8 ± 3 and 9 ± 3 nm for slabs synthesized on PFC and on PTFE, respectively, showing that the particle size in the final slabs was the same. However, the average nanoparticle diameters observed from TEM were larger than the manufacturer-specified nanoparticle diameter of 5 nm. This observation is likely due to the growth of silica nanoparticles in solution caused by Ostwald ripening.[25] The latter is enhanced by the high pH around 9−10 used to stabilize the colloidal solution.[25] Figure 3 also shows that the size of the mesopores between the silica nanoparticles was comparable to the size of nanoparticles; i.e., no large pores were observed, and the slab's mesostructure and appearance were fairly uniform across the image.

Figure 4 shows (a) representative nitrogen adsorption−desorption isotherms and (b) the corresponding pore size distributions for nanoparticle-based mesoporous silica monolithic slabs prepared on PFC liquid and on PTFE. Both isotherms were of type IV with an H2(b) hysteresis loop according to the IUPAC classification.[52,53] Figure 4a indicates that all slabs were mesoporous and had complex pore structures made of interconnected pores with different pore sizes that may have resulted in pore blockage.[52,53] In addition, Figure 4b indicates that the slabs had both homogeneous and fairly small mesopores, with widths between 2 and 10 nm. Note also that the porosity in both samples was nearly identical despite the fact that the SiO_2-PFC-rt slab was calcined.

DOI: 10.1021/acsanm.9b00903
ACS Appl. Nano Mater. 2019, 2, 4547−4555

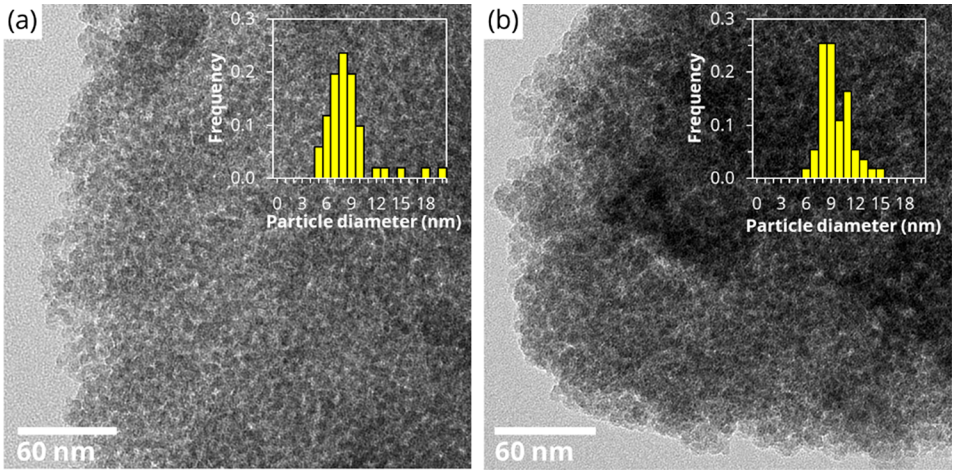

Figure 3. Representative transmission electron microscopy images and measured particle diameter histograms (insets) of nanoparticle-based mesoporous silica monolithic slabs: (a) SiO_2-PFC-rt and (b) SiO_2-PTFE-rt.

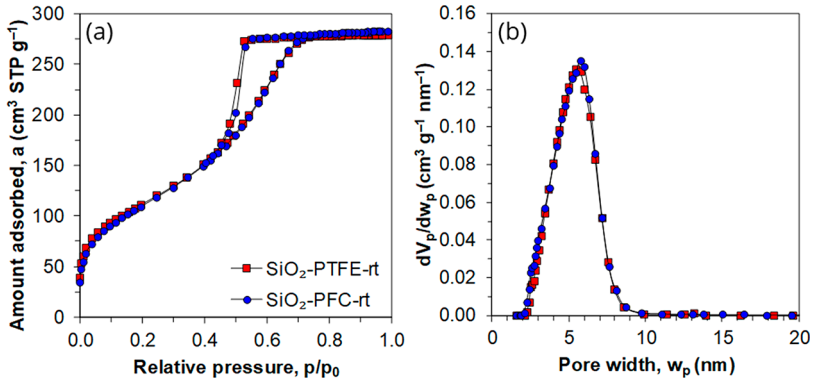

Figure 4. (a) Representative nitrogen adsorption−desorption isotherms and (b) the corresponding adsorption pore size distributions of nanoparticle-based mesoporous silica monolithic slabs synthesized on PFC liquid (SiO_2-PFC-rt) and PTFE (SiO_2-PTFE-rt) and dried at room temperature. Note that only SiO_2-PFC-rt slab was calcined at 400 °C for 2 h.

Table 1. Structural and Optical Characteristics of Nanoparticle-Based Mesoporous Silica Slabs Synthesized on PFC Liquid and on PTFE

sample	average thickness, $\bar{t}$ (mm)	specific surface area, S_{BET} (m^2 g^{-1})	porosity, ϕ	total pore volume, V_t (cm^3 g^{-1})	micropore volume, V_{mi} (cm^3 g^{-1})	peak pore width, w_p (nm)	transmittance, $T_{nh,500}$ (%)	haze, h_{500} (%)	color rendering index (CRI)
SiO_2-PFC-rt	3.5[a]	400[b]	0.46[b]	0.38[b]	0.00[b]	5.0[b]	92[a]	3.8[a]	97[a]
SiO_2-PFC-hc	1.4[a]	360[b]	0.49[b]	0.44[b]	0.00[b]	5.8[b]	97[a]	0.8[a]	98[a]
SiO_2-PFC-40C	1.7	370	0.54	0.53	0.00	7.2	92	2.6	99
SiO_2-PTFE-rt	2.3	390	0.48	0.42	0.01	6.1	93	3.1	98
SiO_2-PTFE-hc	2.7	390	0.47	0.41	0.00	5.5	91	6.6	98
SiO_2-PTFE-40C	1.9	380	0.56	0.57	0.00	7.6	91	10.5	98

[a]Measurements done on two different samples. [b]Measurements done on two different samples.

Table 1 summarizes the structural properties of the mesoporous silica monolithic slabs synthesized on PFC liquid and on PTFE and dried by using different conditions. All slabs dried under the same conditions had similar specific surface area, porosity, and pore width, regardless of the substrate used. Notably, the slabs dried at 40 °C had larger porosity and pore width compared with those dried at room temperature. These differences were attributed to the fact that slabs dried at 40 °C benefitted from additional aging, compared with those dried at room temperature, due to the increased solubility and rates of dissolution and reprecipitation of silica at higher temperature.[25] Drying at 40 °C thus produced stronger silica network that could sustain the capillary forces caused by solvent evaporation during drying. This stronger network did not shrink as much as others, resulting in the largest porosity.

Figure 5a shows representative SAXS patterns plotted as scattering intensity (in au) as a function of scattering vector Q (defined as $2\pi/d$ and having units of nm^{-1}) for mesoporous silica monolithic slabs synthesized on PFC liquid (SiO_2-PFC-rt) and on PTFE (SiO_2-PTFE-rt) and dried at room temperature. SAXS patterns of both slabs consist of (a) Guinier region for $Q < 0.4$ nm^{-1}, (b) weak correlation peaks in the range of $Q = 0.4-1.0$ nm^{-1}, and (c) a Porod region for $Q > 1.0$ nm^{-1}. The presence of Guinier and Porod regions indicates a fractal structure made of aggregated nanoparticles.[54] The weak correlation peaks indicate limited pore-to-pore correla-

DOI: 10.1021/acsanm.9b00903
ACS Appl. Nano Mater. 2019, 2, 4547−4555

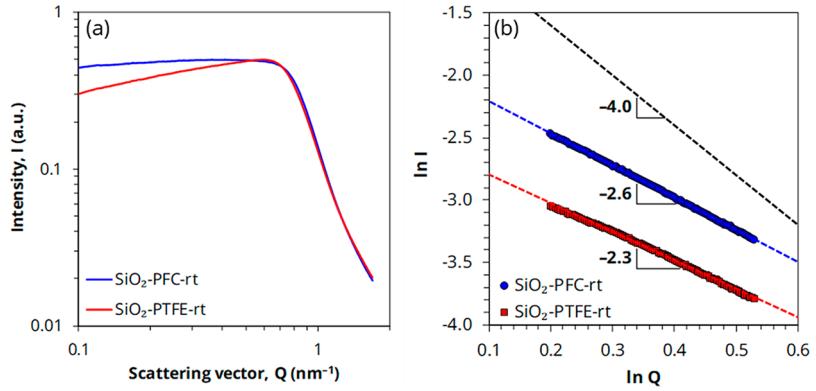

Figure 5. (a) Representative small-angle X-ray scattering patterns of nanoparticle-based mesoporous silica monolithic slabs synthesized on PFC liquid (SiO_2-PFC-rt) and on PTFE (SiO_2-PTFE-rt) and (b) corresponding Porod plots obtained after subtracting contributions from disordered worm-like mesopores. The black dashed line with a slope of −4 corresponds to the behavior of nonfractal materials obeying the Porod's law.[54] Intensity scales in both panels are in arbitrary units.

Table 2. Average and Root-Mean-Squared Surface Roughness of Thick Transparent Nanoparticle-Based Mesoporous Silica Slabs Synthesized on PFC Liquid and on PTFE along with Float Soda Lime Glass

	SiO_2-PFC		SiO_2-PTFE		
	top	bottom	top	bottom	float glass
R_a (nm)	15.5 ± 1.0	13 ± 9	4.5 ± 0.2	140 ± 9	1.6 ± 0.1
R_{rms} (nm)	20.3 ± 0.9	18.6 ± 1.3	8 ± 2	175 ± 13	2.1 ± 0.2

tion due to the narrow pore size distribution and the uniform pore wall thickness.[55] However, the low intensity of these peaks and lack of high-order diffraction peaks indicate that pores lacked long-range order and most likely formed a disordered worm-like porous structure.[55] A worm-like pore structure is consistent with the type IV isotherm with a H2(b) hysteresis loop observed in both nitrogen adsorption−desorption isotherms presented in Figure 4.[52,53]

Figure 5b shows Porod plots and their slopes for both slabs shown in Figure 5a, obtained after subtracting correlation contributions from disordered worm-like mesopores (see the Supporting Information for details of the analysis). In the Porod region, the scattering intensity I relates to the scattering vector modulus Q according to the power law[54]

$$I \sim Q^{-D} \quad (1)$$

Here, a power law exponent $D < 3$ indicates a mass fractal structure with a mass fractal dimension $D_m = D$ while $3 < D < 4$ indicates a surface fractal structure with a surface fractal dimension $D_s = 6 - D$, and $D > 4$ indicates a nonfractal structure.[54] The mass fractal dimension D_m quantifies how the mass of a fractal structure increases with its increasing size[54]

$$m \sim r^{D_m} \quad (2)$$

where m is the mass contained in a sphere of mesoporous material of radius r. Notably, the mass fractal dimension D_m can be fractional and ranges from 1 to 3.[54] Figure 5b shows that both SiO_2-PFC-rt and SiO_2-PTFE-rt slabs have mass fractal structures, but with different mass fractal dimensions. For SiO_2-PFC-rt $D_m = 2.6$ while SiO_2-PTFE-rt has a lower value of $D_m = 2.3$.

Mesoporous silica prepared through the sol−gel process are typically mass fractal structures due to their kinetically controlled growth.[25] The latter proceeds either by monomer−cluster aggregation or cluster−cluster aggregation.[25] In monomer−cluster aggregation, the fractal structure grows by gradual addition of nanoparticles to existing clusters of aggregated nanoparticles, while in cluster−cluster aggregation, all nanoparticles aggregate randomly at roughly the same time, forming clusters that grow by colliding with other clusters.[25] Notably, monomer−cluster aggregation produces mass fractal structures with higher mass fractal dimension than cluster−cluster aggregation.[25] We speculate that the higher mass fractal dimension of the SiO_2-PFC-rt slabs was due to slight solubility of PFC liquid in the colloidal solution of silica nanoparticles.[56−58] Any dissolved hydrophobic PFC molecules interacted with or adsorbed onto the silica nanoparticles, thus destabilizing the nanoparticle suspension. As a result, some silica nanoparticles started aggregating early in the drying process, resulting in the formation of a small number of clusters that then gradually grew by addition of nanoparticles from the solution. Thus, SiO_2-PFC slabs may grow more through monomer−cluster aggregation than SiO_2-PTFE, resulting in a higher mass fractal dimension.

3.3. Surface Roughness. For any optical applications, clarity is a key concern, and surface roughness can be a major source of scattering. Table 2 summarizes the average and root-mean-squared (rms) surface roughness of the two faces of nanoparticle-based mesoporous SiO_2-PFC and SiO_2-PTFE slabs along with that of commercial float glass obtained from Nippon Sheet Glass (Japan), used as a reference. While the top surface of the SiO_2-PTFE slabs was optically smooth (R_a = 4.5 ± 0.2 nm), the bottom surface, which was in contact with the PTFE mold, had a much higher roughness R_a = 140 ± 9 nm, comparable to the wavelength of visible light. This roughness was caused by the roughness of the PTFE substrate imprinted onto the slab's bottom surface during gel formation (Figure S2b). By contrast, both the top and bottom surfaces of the SiO_2-PFC slabs were optically smooth with surface roughness between 13.4 and 15.5 nm (Figure S2a). In fact, the surface in contact with the PFC liquid substrate was as smooth as the top surface. Note that the SiO_2-PFC slabs had rougher top surface

DOI: 10.1021/acsanm.9b00903
ACS Appl. Nano Mater. 2019, 2, 4547−4555

than the SiO_2-PTFE slabs possibly due to the different aggregation mechanisms of silica nanoparticles during gelation of both slabs as discussed in section 3.2. As a reference, soda lime sheet glass had a surface roughness 10 times smaller than that of the mesoporous SiO_2-PFC slabs (R_a = 1.6 ± 0.1 nm) resulting from the float glass process on liquid tin.[59,60]

Another challenge for the SiO_2-PTFE slabs is that scratches and defects in the PTFE substrate resulted in the formation of air bubbles at the bottom surface of some SiO_2-PTFE slabs (Figure S3a). The scratches and defects acted as nucleation sites for bubbles formation from gases dissolved in the colloidal solution (Figure S3b). These bubbles strongly scattered light due to their large diameter, ranging between 0.1 and 1 mm. Both surface roughness and bubble nucleation were minimized either when PTFE molds with extremely smooth surfaces were used (Figure S3) or for all slabs synthesized on PFC liquid substrates (Figure 2a and Figure S1).

3.4. Optical Characterization. We used transmittance and haze measurements in the visible range and color rendering index to characterize the optical transparency of our mesoporous silica slabs. Figure 6 shows the spectral

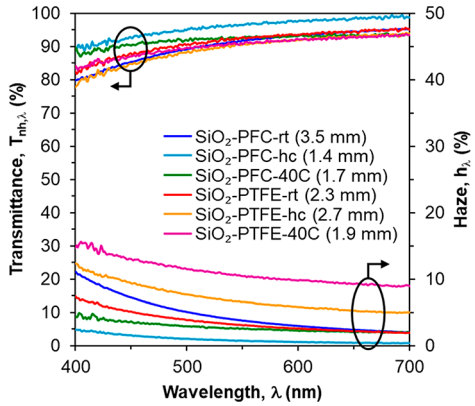

Figure 6. Spectral normal-hemispherical transmittance $T_{nh,\lambda}$ and haze h_λ of thick transparent nanoparticle-based mesoporous silica slabs synthesized on PFC liquid and on PTFE. The average thickness of the slabs is indicated in parentheses.

normal-hemispherical transmittance and haze for thick transparent nanoparticle-based mesoporous silica slabs synthesized on PFC liquid and on PTFE. Table 1 summarizes the normal-hemispherical transmittance and haze at wavelength λ = 500 nm for the different slabs synthesized in this study. It indicates that the SiO_2-PFC slabs generally had similar normal-hemispherical transmittance $T_{nh,500}$ and lower haze h_{500} than the SiO_2-PTFE slabs. For example, the SiO_2-PFC-40C slab had similar normal-hemispherical transmittance ($T_{nh,500}$ = 92%) and lower haze (h_{500} = 2.6%) than the SiO_2-PTFE-40C slab ($T_{nh,500}$ = 91%, h_{500} = 10.5%), despite the fact that both slabs had similar thickness of 1.7−1.9 mm. Moreover, the 3.5 mm thick SiO_2-PFC-rt slab had similar normal-hemispherical transmittance ($T_{nh,500}$ = 92%) and lower haze (h_{500} = 3.8%) than the 2.7 mm thick SiO_2-PTFE-hc slab ($T_{nh,500}$ = 91% and h_{500} = 6.6%), despite the fact that the SiO_2-PFC-rt slab had significantly larger thickness. The high spectral normal-hemispherical transmittance and low haze of SiO_2-PFC slabs were attributed to (i) their small nanoparticle size (Figure 3), (ii) their small pore size and narrow pore size distribution (Figure 4b), and (iii) their optically smooth top and bottom surfaces (Table 2), which minimized both volumetric and surface light scattering. The differences in transmittance and haze between samples synthesized on PFC liquid and PTFE substrates with similar porosity and pore size distribution can mainly be attributed to differences in the slab surface roughness, which was responsible for stronger scattering and haze in SiO_2-PTFE slabs. Finally, all slabs listed in Table 1 had color rendering index exceeding 98, indicating excellent reproduction of colors.

3.5. Thermal Characterization. The goal of this work is to achieve mesoporous silica monolithic slabs with high optical transparency and low thermal conductivity. Here, we used time-domain thermoreflectance to measure the effective thermal conductivity of the slabs. The mesoporous SiO_2-PFC-hc slab had an effective thermal conductivity of 104 ± 15 mW m^{-1} K^{-1} at room temperature in air at atmospheric pressure while that of mesoporous SiO_2-PTFE-rt slab was 160 ± 20 mW m^{-1} K^{-1} at room temperature in a vacuum for similar porosity around 49%. While these two samples have slightly different drying conditions, they were both dried at room temperature, and they were selected for comparison because they had the most similar porosity among all the slabs. Other SiO_2-PFC and SiO_2-PTFE slabs had more variation in porosity, which is known to strongly affect the effective thermal conductivity.[29] The difference in effective thermal conductivity despite similar porosity and pore size distribution (Figure 4) is likely due to the difference in mass fractal dimension between SiO_2-PFC and SiO_2-PTFE slabs, as determined by SAXS (Figure 5). Indeed, Emmerling and Fricke[61] showed that the effective thermal conductivity of nanoparticle-based mesoporous silica with a mass fractal structure can be expressed as

$$\frac{k_{eff}}{k_{SiO_2}} \sim \left(\frac{\rho_{eff}}{\rho_{SiO_2}}\right)^{\nu} \tag{3}$$

where k_{eff} and ρ_{eff} are the effective thermal conductivity and effective density of the fractal nanoparticle-based mesoporous silica, and k_{SiO_2} and ρ_{SiO_2} are the thermal conductivity and density of the solid silica backbone. Here, $\nu = \frac{1}{2}\left(\frac{5-D_m}{3-D_m}\right)$ is a scaling factor, expressed as a function of the mass fractal dimension D_m. Note that $\nu \geq 1$, since $1 < D_m < 3$, and that ν increases monotonically with increasing D_m. Therefore, based on eq 3, the effective thermal conductivity of a nanoparticle-based mesoporous silica with a mass fractal structure should decrease with increasing mass fractal dimension. Thus, the SiO_2-PFC slabs should have a lower effective thermal conductivity than the SiO_2-PTFE slabs due to their higher mass fractal dimension of D_m = 2.6 compared to 2.3 for the SiO_2-PTFE slabs.

Importantly, both types of nanoparticle-based mesoporous silica slabs synthesized in this study had effective thermal conductivity somewhat smaller than those reported in the literature for other silica-based materials with similar porosity.[29] For example, Coquil et al.[29] synthesized mesoporous silica thin films on Si substrates with hexagonally ordered cylindrical pores using TEOS as the silica precursor and Pluronic P123 block copolymer as the template. The films featured porosity of 40−48% and effective cross-plane thermal conductivities of 220−180 mW m^{-1} K^{-1}. Note that those films did not have a mass fractal structure because they lacked the required structural self-similarity[54] due to their hexagonally ordered and uniform mesoporous structure. Thus, the fractal

DOI: 10.1021/acsanm.9b00903
ACS Appl. Nano Mater. 2019, 2, 4547−4555

structure of our slabs, regardless of the substrate used during synthesis, appears to lead to a lower effective thermal conductivity across all samples. For further comparison, Günay et al.[24] synthesized hydrophobic silica aerogel slabs for solar−thermal energy conversion with very high porosity ≈93% and an effective thermal conductivity of 130 ± 30 mW m^{-1} K^{-1}. For comparison, our nanoparticle-based mesoporous SiO_2-PFC slabs had a lower effective thermal conductivity of only 104 ± 15 mW m^{-1} K^{-1}, despite significantly lower porosity around 50%. This result indicates that the present nanoparticle-based mesoporous silica slabs are also promising candidates for solar−thermal energy conversion.

3.6. Mechanical Characterization. Table 3 summarizes the Young's modulus and hardness of thick transparent nanoparticle-based mesoporous silica slabs synthesized on PFC liquid and on PTFE at room temperature. It is interesting to note that the SiO_2-PFC-rt slabs had Young's moduli and hardness values slightly smaller than those of SiO_2-PTFE-rt slabs, despite the fact that all slabs had similar porosity around 0.47. The difference in mechanical properties was likely again due to the difference in mass fractal dimension between the SiO_2-PFC and SiO_2-PTFE slabs. Indeed, Emmerling and Fricke[61] showed that the effective Young's modulus of nanoparticle-based mesoporous silica with a mass fractal structure can be expressed as

Table 3. Measured Effective Young's modulus and Hardness of Thick Transparent Nanoparticle-Based Mesoporous Silica Slabs Synthesized on PFC Liquid and on PTFE

sample	porosity, ϕ	Young's modulus, E_{eff} (GPa)	hardness, H_{eff} (GPa)
SiO_2-PFC-rt	0.46	5.4	0.42
SiO_2-PFC-rt	0.47	5.7	0.47
SiO_2-PTFE-rt	0.46	6.2	0.51
SiO_2-PTFE-rt	0.47	6.9	0.69
SiO_2-PTFE-rt	0.49	6.0	0.51

$$\frac{E_{eff}}{E_{SiO_2}} \sim \left(\frac{\rho_{eff}}{\rho_{SiO_2}}\right)^{2\nu} \quad (4)$$

where E_{eff} is the effective Young's modulus of the fractal nanoparticle-based mesoporous silica and E_{SiO_2} is the Young's modulus of the bulk solid silica backbone. Following the argument outlined in section 3.5, eq 4 shows that the effective Young's modulus of nanoparticle-based mesoporous silica with a mass fractal structure decreases with increasing mass fractal dimension D_m. Thus, it is expected that the SiO_2-PFC slabs should have a lower effective Young's modulus than the SiO_2-PTFE slabs due to their higher mass fractal dimension. We speculate that the same reasoning and behavior is valid for hardness.

Overall, the measured effective Young's moduli E_{eff} of 5.4−6.9 GPa and hardness values H_{eff} of 0.42−0.69 GPa are consistent with those reported for other mesoporous silica with similar porosity.[62,63] Moreover, the Young's moduli and hardness values of the synthesized slabs are superior to those reported for common polymers such as poly(vinyl chloride) (PVC) (E = 2.64 ± 0.10 GPa, H = 0.138−0.347 GPa) and poly(methyl methacrylate) (PMMA) (E = 2.34 ± 0.15 GPa, H = 0.222−0.278 GPa).[64]

4. CONCLUSION

This paper presented a novel template-free water-based sol−gel method to synthesize thick, optically transparent, and thermally insulating mesoporous silica monolithic slabs under ambient conditions. For the first time, mesoporous silica slabs were synthesized on PFC liquid substrates (1) to reduce adhesion between gel and substrate, enabling the gels to shrink freely during aging and drying without incurring significant stress that would otherwise lead to fractures, and (2) to provide a smooth interface that results in slabs with optically smooth surfaces. The free-standing nanoparticle-based mesoporous silica slabs were made as disks or squares, with thickness between 1 and 6 mm and porosity of 45−55%. The slabs had high normal-hemispherical transmittance (>85%) and low haze (<5%) in the visible region of the spectrum due to small nanoparticle size, small pore size, narrow pore size distribution, and optically smooth surfaces, all of which resulted in limited volumetric and surface light scattering. The lowest effective thermal conductivity achieved was 104 ± 15 mW m^{-1} K^{-1}, and the mechanical properties are superior to common polymers such as PVC and PMMA. Most notable, however, is the fact that the slabs synthesized in this study had effective thermal conductivity smaller than those reported in the literature for other mesoporous silica materials with similar or larger porosity. This was attributed to the fractal structure and the high mass fractal dimension of the slabs synthesized in this study as established by small-angle X-ray scattering. Overall, the present nanoparticle-based mesoporous silica slabs are promising candidates for optically transparent and thermally insulating materials in window solutions and solar−thermal energy conversion, for example.

■ ASSOCIATED CONTENT

Supporting Information

The Supporting Information is available free of charge on the ACS Publications website at DOI: 10.1021/acsanm.9b00903.

Experimental details and additional optical images (PDF)

■ AUTHOR INFORMATION

Corresponding Author

*E-mail: pilon@seas.ucla.edu.

ORCID

Michal Marszewski: 0000-0002-4157-3046
Bruce Dunn: 0000-0001-5669-4740
Sarah H. Tolbert: 0000-0001-9969-1582
Laurent Pilon: 0000-0001-9459-8207

Notes

The authors declare no competing financial interest.

■ ACKNOWLEDGMENTS

This research was supported in part by Advanced Research Projects Agency-Energy (ARPA-E) Single-Pane Highly Insulating Efficient Lucid Designs (SHIELD) program (ARPA-E Award DE-AR0000738). The authors acknowledge the use of instruments at the Electron Imaging Center for NanoMachines supported by NIH (1S10RR23057 to ZHZ) and CNSI at UCLA. Use of the Stanford Synchrotron Radiation Lightsource, SLAC National Accelerator Laboratory, is supported by the U.S. Department of Energy, Office of Science, Office of Basic Energy Sciences, under Contract DE-AC02-76SF00515.

DOI: 10.1021/acsanm.9b00903
ACS Appl. Nano Mater. 2019, 2, 4547−4555

The authors are grateful to Nalco Chemical Company (Naperville, IL) for generously providing aqueous suspension of silica nanoparticles Nalco 2326 and to Nippon Sheet Glass for provided samples of float soda lime silicate glass.

NOMENCLATURE

a amount adsorbed (cm^3 STP g^{-1})
CRI color rendering index
d interplanar spacing (nm)
D Porod exponent
D_m mass fractal dimension
D_s surface fractal dimension
E Young's modulus (GPa)
h haze (%)
H hardness (GPa)
I intensity (au)
k thermal conductivity (W m^{-1} K^{-1})
m mass (kg)
p pressure (Pa)
p_0 saturation pressure (Pa)
Q scattering vector (nm^{-1})
r radius (m)
R_a average surface roughness (nm)
R_{rms} root-mean-squared surface roughness (nm)
S_{BET} specific surface area (m^2 g^{-1})
t average thickness (mm)
T_{nh} normal-hemispherical transmittance (%)
V_{mi} micropore volume (cm^3 g^{-1})
V_p cumulative pore volume (cm^3 g^{-1})
V_t total pore volume (cm^3 g^{-1})
w_p pore width (nm)

Greek Symbols

λ wavelength (nm)
ν scaling factor
ρ density (g cm^{-3})
ϕ porosity

Subscripts and Superscripts

eff refers to effective
SiO_2 refers to silica

REFERENCES

(1) Kirkbir, F.; Murata, H.; Meyers, D.; Chaudhuri, S. R.; Sarkar, A. Drying and Sintering of Sol-Gel Derived Large SiO_2 Monoliths. *J. Sol-Gel Sci. Technol.* **1996**, *6* (3), 203−217.
(2) Soleimani Dorcheh, A.; Abbasi, M. H. Silica Aerogel; Synthesis, Properties and Characterization. *J. Mater. Process. Technol.* **2008**, *199* (1), 10−26.
(3) Sun, Z.; Deng, Y.; Wei, J.; Gu, D.; Tu, B.; Zhao, D. Hierarchically Ordered Macro-/Mesoporous Silica Monolith: Tuning Macropore Entrance Size for Size-Selective Adsorption of Proteins. *Chem. Mater.* **2011**, *23* (8), 2176−2184.
(4) Tao, S.; Wang, Y.; An, Y. Superwetting Monolithic SiO_2 with Hierarchical Structure for Oil Removal. *J. Mater. Chem.* **2011**, *21* (32), 11901−11907.
(5) Rodrigues, D.; Rocha-Santos, T. A. P.; Freitas, A. C.; Gomes, A. M. P.; Duarte, A. C. Strategies Based on Silica Monoliths for Removing Pollutants from Wastewater Effluents: A Review. *Sci. Total Environ.* **2013**, *461*−*462*, 126−138.
(6) Galarneau, A.; Sachse, A.; Said, B.; Pelisson, C.-H.; Boscaro, P.; Brun, N.; Courtheoux, L.; Olivi-Tran, N.; Coasne, B.; Fajula, F. Hierarchical Porous Silica Monoliths: A Novel Class of Microreactors for Process Intensification in Catalysis and Adsorption. *C. R. Chim.* **2016**, *19* (1), 231−247.
(7) Ren, L.-H.; Zhang, H.-L.; Lu, A.-H.; Hao, Y.; Li, W.-C. Porous Silica as Supports for Controlled Fabrication of $Au/CeO_2/SiO_2$ Catalysts for CO Oxidation: Influence of the Silica Nanostructures. *Microporous Mesoporous Mater.* **2012**, *158*, 7−12.
(8) Haas, C. P.; Mullner, T.; Kohns, R.; Enke, D.; Tallarek, U. High-Performance Monoliths in Heterogeneous Catalysis with Single-Phase Liquid Flow. *React. Chem. Eng.* **2017**, *2* (4), 498−511.
(9) Galarneau, A.; Iapichella, J.; Brunel, D.; Fajula, F.; Bayram-Hahn, Z.; Unger, K.; Puy, G.; Demesmay, C.; Rocca, J.-L. Spherical Ordered Mesoporous Silicas and Silica Monoliths as Stationary Phases for Liquid Chromatography. *J. Sep. Sci.* **2006**, *29* (6), 844−855.
(10) Zhong, H.; Zhu, G.; Wang, P.; Liu, J.; Yang, J.; Yang, Q. Direct Synthesis of Hierarchical Monolithic Silica for High Performance Liquid Chromatography. *J. Chromatogr. A* **2008**, *1190* (1), 232−240.
(11) Wang, S.-T.; Wang, M.-Y.; Su, X.; Yuan, B.-F.; Feng, Y.-Q. Facile Preparation of SiO_2/TiO_2 Composite Monolithic Capillary Column and Its Application in Enrichment of Phosphopeptides. *Anal. Chem.* **2012**, *84* (18), 7763−7770.
(12) Meinusch, R.; Hormann, K.; Hakim, R.; Tallarek, U.; Smarsly, B. M. Synthesis and Morphological Characterization of Phenyl-Modified Macroporous-Mesoporous Hybrid Silica Monoliths. *RSC Adv.* **2015**, *5* (26), 20283−20294.
(13) Nuzhdin, A. L.; Shalygin, A. S.; Artiukha, E. A.; Chibiryaev, A. M.; Bukhtiyarova, G. A.; Martyanov, O. N. HKUST-1 Silica Aerogel Composites: Novel Materials for the Separation of Saturated and Unsaturated Hydrocarbons by Conventional Liquid Chromatography. *RSC Adv.* **2016**, *6* (67), 62501−62507.
(14) Yazawa, T.; Machida, F.; Kubo, N.; Jin, T. Photocatalytic Activity of Transparent Porous Glass Supported TiO_2. *Ceram. Int.* **2009**, *35* (8), 3321−3325.
(15) Subbiah, S.; Mokaya, R. Transparent Thin Films and Monoliths Synthesized from Fullerene Doped Mesoporous Silica: Evidence for Embedded Monodispersed C_{60}. *Chem. Commun.* **2003**, *0* (1), 92−93.
(16) Murai, S.; Fujita, K.; Nakanishi, K.; Hirao, K. Fabrication of Dye-Infiltrated Macroporous Silica for Laser Amplification. *J. Non-Cryst. Solids* **2004**, *345*−*346*, 438−442.
(17) Schmidt, M.; Boettger, G.; Eich, M.; Morgenroth, W.; Huebner, U.; Boucher, R.; Meyer, H. G.; Konjhodzic, D.; Bretinger, H.; Marlow, F. Ultralow Refractive Index Substrates-a Base for Photonic Crystal Slab Waveguides. *Appl. Phys. Lett.* **2004**, *85* (1), 16−18.
(18) Wittwer, V. Development of Aerogel Windows. *J. Non-Cryst. Solids* **1992**, *145*, 233−236.
(19) Jensen, K. I.; Schultz, J. M.; Kristiansen, F. H. Development of Windows Based on Highly Insulating Aerogel Glazings. *J. Non-Cryst. Solids* **2004**, *350*, 351−357.
(20) Nordgaard, A.; Beckman, W. Modeling of Flat-Plate Collectors Based on Monolithic Silica Aerogel. *Sol. Energy* **1992**, *49* (5), 387−402.
(21) Weinstein, L. A.; Loomis, J.; Bhatia, B.; Bierman, D. M.; Wang, E. N.; Chen, G. Concentrating Solar Power. *Chem. Rev.* **2015**, *115* (23), 12797−12838.
(22) McEnaney, K.; Weinstein, L.; Kraemer, D.; Ghasemi, H.; Chen, G. Aerogel-Based Solar Thermal Receivers. *Nano Energy* **2017**, *40*, 180−186.
(23) Strobach, E.; Bhatia, B.; Yang, S.; Zhao, L.; Wang, E. N. High Temperature Annealing for Structural Optimization of Silica Aerogels in Solar Thermal Applications. *J. Non-Cryst. Solids* **2017**, *462*, 72−77.
(24) Günay, A. A.; Kim, H.; Nagarajan, N.; Lopez, M.; Kantharaj, R.; Alsaati, A.; Marconnet, A.; Lenert, A.; Miljkovic, N. Optically Transparent Thermally Insulating Silica Aerogels for Solar Thermal Insulation. *ACS Appl. Mater. Interfaces* **2018**, *10* (15), 12603−12611.
(25) Brinker, C. J.; Scherer, G. W. *Sol-Gel Science: The Physics and Chemistry of Sol-Gel Processing*; Academic Press: Boston, 1990.
(26) Wan, Y.; Zhao, D. On the Controllable Soft-Templating Approach to Mesoporous Silicates. *Chem. Rev.* **2007**, *107* (7), 2821−2860.
(27) Cao, L.; Man, T.; Kruk, M. Synthesis of Ultra-Large-Pore SBA-15 Silica with Two-Dimensional Hexagonal Structure Using

DOI: 10.1021/acsanm.9b00903
ACS Appl. Nano Mater. 2019, 2, 4547−4555

Triisopropylbenzene As Micelle Expander. *Chem. Mater.* **2009**, *21* (6), 1144−1153.
(28) Rubin, M.; Lampert, C. M. Transparent Silica Aerogels for Window Insulation. *Sol. Energy Mater.* **1983**, *7* (4), 393−400.
(29) Coquil, T.; Richman, E. K.; Hutchinson, N. J.; Tolbert, S. H.; Pilon, L. Thermal Conductivity of Cubic and Hexagonal Mesoporous Silica Thin Films. *J. Appl. Phys.* **2009**, *106* (3), 034910.
(30) Galy, T.; Mu, D.; Marszewski, M.; Pilon, L. Computer-Generated Mesoporous Materials and Associated Structural Characterization. *Comput. Mater. Sci.* **2019**, *157*, 156−167.
(31) Pajonk, G. M. Transparent Silica Aerogels. *J. Non-Cryst. Solids* **1998**, *225*, 307−314.
(32) Smith, D. M.; Deshpande, R.; Brinke, C. J. Preparation of Low-Density Aerogels at Ambient Pressure. *MRS Online Proc. Libr. Arch.* **1992**, DOI: 10.1557/PROC-271-567.
(33) Smith, D. M.; Stein, D.; Anderson, J. M.; Ackerman, W. Preparation of Low-Density Xerogels at Ambient Pressure. *J. Non-Cryst. Solids* **1995**, *186*, 104−112.
(34) Land, V. D.; Harris, T. M.; Teeters, D. C. Processing of Low-Density Silica Gel by Critical Point Drying or Ambient Pressure Drying. *J. Non-Cryst. Solids* **2001**, *283* (1), 11−17.
(35) Kim, G.-S.; Hyun, S.-H. Synthesis of Window Glazing Coated with Silica Aerogel Films via Ambient Drying. *J. Non-Cryst. Solids* **2003**, *320* (1), 125−132.
(36) Chen, K.; Bao, Z.; Du, A.; Zhu, X.; Shen, J.; Wu, G.; Zhang, Z.; Zhou, B. One-Pot Synthesis, Characterization and Properties of Acid-Catalyzed Resorcinol/Formaldehyde Cross-Linked Silica Aerogels and Their Conversion to Hierarchical Porous Carbon Monoliths. *J. Sol-Gel Sci. Technol.* **2012**, *62* (3), 294−303.
(37) Ikeda, H.; Fujino, S. Composition and PH Dependence on Aggregation of SiO_2-PVA Suspension for the Synthesis of Porous SiO_2-PVA Nanocomposite. *J. Porous Mater.* **2014**, *21* (6), 1143−1149.
(38) Grund, S.; Seifert, A.; Baumann, G.; Baumann, W.; Marx, G.; Kehr, M.; Spange, S. Monolithic Silica with Bimodal Pore Size Distribution Fabricated by Self-Separated Sol-Gel Composite Materials. *Microporous Mesoporous Mater.* **2006**, *95* (1), 206−212.
(39) Guillemot, F.; Brunet-Bruneau, A.; Bourgeat-Lami, E.; Boilot, J.-P.; Barthel, E.; Gacoin, T. Percolation Transition in the Porous Structure of Latex-Templated Silica Monoliths. *Microporous Mesoporous Mater.* **2013**, *172*, 146−150.
(40) Shi, Z.-G.; Xu, L.-Y.; Feng, Y.-Q. A New Template for the Synthesis of Porous Inorganic Oxide Monoliths. *J. Non-Cryst. Solids* **2006**, *352* (38), 4003−4007.
(41) Zhang, X.; Jing, S.; Chen, Z.; Zhong, L.; Liu, Q.; Peng, X.; Sun, R. Fabricating 3D Hierarchical Porous TiO_2 and SiO_2 with High Specific Surface Area by Using Nanofibril-Interconnected Cellulose Aerogel as a New Biotemplate. *Ind. Crops Prod.* **2017**, *109*, 790−802.
(42) Tang, X.; Sun, A.; Chu, C.; Yu, M.; Ma, S.; Cheng, Y.; Guo, J.; Xu, G. A Novel Silica Nanowire-Silica Composite Aerogels Dried at Ambient Pressure. *Mater. Des.* **2017**, *115*, 415−421.
(43) Hwang, S.-W.; Kim, T.-Y.; Hyun, S.-H. Optimization of Instantaneous Solvent Exchange/Surface Modification Process for Ambient Synthesis of Monolithic Silica Aerogels. *J. Colloid Interface Sci.* **2008**, *322* (1), 224−230.
(44) Kanamori, K.; Nakanishi, K. Controlled Pore Formation in Organotrialkoxysilane-Derived Hybrids: From Aerogels to Hierarchically Porous Monoliths. *Chem. Soc. Rev.* **2011**, *40* (2), 754−770.
(45) Yang, Y.; Shi, E.; Li, P.; Wu, D.; Wu, S.; Shang, Y.; Xu, W.; Cao, A.; Yuan, Q. A Compressible Mesoporous SiO_2 Sponge Supported by a Carbon Nanotube Network. *Nanoscale* **2014**, *6* (7), 3585−3592.
(46) Zu, G.; Shimizu, T.; Kanamori, K.; Zhu, Y.; Maeno, A.; Kaji, H.; Shen, J.; Nakanishi, K. Transparent, Superflexible Doubly Cross-Linked Polyvinylpolymethylsiloxane Aerogel Superinsulators via Ambient Pressure Drying. *ACS Nano* **2018**, *12* (1), 521−532.
(47) Prakash, S. S.; Brinker, C. J.; Hurd, A. J.; Rao, S. M. Silica Aerogel Films Prepared at Ambient Pressure by Using Surface Derivatization to Induce Reversible Drying Shrinkage. *Nature* **1995**, *374* (6521), 439−443.
(48) Roziere, J.; Brandhorst, M.; Dutartre, R.; Jacquin, M.; Jones, D. J.; Vitse, P.; Zajac, J. Effect of Surfactant Type, Substitution by Aluminium and Additives on Direct Liquid Crystal Templated Monolithic Silica. *J. Mater. Chem.* **2001**, *11* (12), 3264−3275.
(49) Yang, H.; Shi, Q.; Tian, B.; Xie, S.; Zhang, F.; Yan; Tu, B.; Zhao, D. A Fast Way for Preparing Crack-Free Mesostructured Silica Monolith. *Chem. Mater.* **2003**, *15* (2), 536−541.
(50) Lei, J.-H.; Liu, D.; Guo, L.-P.; Yan, X.-M.; Tong, H. Fabrication and Characterization of Hexagonal Mesoporous Silica Monolith via Post-Synthesized Hydrothermal Process. *J. Sol-Gel Sci. Technol.* **2006**, *39* (2), 169−174.
(51) Krytox Performance Lubricants Product Information Datasheet, Miller-Stephenson, Inc.
(52) Sing, K. S. W.; Everett, D. H.; Haul, R. A. W.; Moscou, L.; Pierotti, R. A.; Rouquerol, J.; Siemieniewska, T. Reporting Physisorption Data for Gas/Solid Systems with Special Reference to the Determination of Surface Area and Porosity (Recommendations 1984). *Pure Appl. Chem.* **1985**, *57* (4), 603−619.
(53) Thommes, M.; Kaneko, K.; Neimark, A. V.; Olivier, J. P.; Rodriguez-Reinoso, F.; Rouquerol, J.; Sing, K. S. W. Physisorption of Gases, with Special Reference to the Evaluation of Surface Area and Pore Size Distribution (IUPAC Technical Report). *Pure Appl. Chem.* **2015**, *87* (9−10), 1051−1069.
(54) Melnichenko, Y. B. Structural Characterization of Porous Materials Using SAS. In *Small-Angle Scattering from Confined and Interfacial Fluids*; Springer International Publishing: Cham, 2016; pp 139−171.
(55) Pauly, T. R.; Liu, Y.; Pinnavaia, T. J.; Billinge, S. J. L.; Rieker, T. P. Textural Mesoporosity and the Catalytic Activity of Mesoporous Molecular Sieves with Wormhole Framework Structures. *J. Am. Chem. Soc.* **1999**, *121* (38), 8835−8842.
(56) Wen, W.-Y.; Muccitelli, J. A. Thermodynamics of Some Perfluorocarbon Gases in Water. *J. Solution Chem.* **1979**, *8* (3), 225−246.
(57) Schutt, E. G.; Klein, D. H.; Mattrey, R. M.; Riess, J. G. Injectable Microbubbles as Contrast Agents for Diagnostic Ultrasound Imaging: The Key Role of Perfluorochemicals. *Angew. Chem., Int. Ed.* **2003**, *42* (28), 3218−3235.
(58) Riess, J. G. Understanding the Fundamentals of Perfluorocarbons and Perfluorocarbon Emulsions Relevant to *In Vivo* Oxygen Delivery. *Artif. Cells Blood Substit. Biotechnol.* **2005**, *33* (1), 47−63.
(59) Pilkington, L. A. B.; Kenneth, B. Manufacture of Flat Glass. US2911759A, November 10, 1959.
(60) Nascimento, M. L. F. Brief History of the Flat Glass Patent - Sixty Years of the Float Process. *World Pat. Inf.* **2014**, *38*, 50−56.
(61) Emmerling, A.; Fricke, J. Scaling Properties and Structure of Aerogels. *J. Sol-Gel Sci. Technol.* **1997**, *8* (1), 781−788.
(62) Li, X.; Birnbaum, J. C.; Williford, R. E.; Fryxell, G. E.; Coyle, C. A.; Dunham, G. C.; Baskaran, S. Effect of Humidity Treatments on Porosity and Mechanical Integrity of Mesoporous Silica Films. *Chem. Commun.* **2003**, *0* (16), 2054−2055.
(63) Yamada, K.; Oku, Y.; Hata, N.; Seino, Y.; Negoro, C.; Kikkawa, T. Structural and Electrical Properties of Ultralow-k, Disordered Mesoporous Silica Films Synthesized Using Nonionic Templates. *J. Electrochem. Soc.* **2004**, *151* (10), F248−F251.
(64) Amitay-Sadovsky, E.; Wagner, H. D. Evaluation of Young's Modulus of Polymers from Knoop Microindentation Tests. *Polymer* **1998**, *39* (11), 2387−2390.

DOI: 10.1021/acsanm.9b00903
ACS Appl. Nano Mater. 2019, 2, 4547−4555